Mon. Not. R. Astron. Soc. **000**, 1–17 (2009) Printed 23 November 2009 (MN LaTeX style file v2.2)

arXiv:0902.1754v2 [astro-ph.GA] 23 Nov 2009

Formation of Isolated Dwarf Galaxies with Feedback

Till Sawala[1⋆], Cecilia Scannapieco[1], Umberto Maio[2] and Simon White[1]
[1] *Max-Planck Institute for Astrophysics, Karl-Schwarzschild-Strasse 1, 85748 Garching, Germany*
[2] *Max-Planck Institute for Extraterrestrial Physics, Giessenbachstrasse 1, 85748 Garching, Germany*

Accepted 2009 January 1. Received 2009 January 1; in original form 2009 January 1

ABSTRACT

We present results of high resolution hydrodynamical simulations of the formation and evolution of dwarf galaxies. Our simulations start from cosmological initial conditions at high redshift. They include metal-dependent cooling, star formation, feedback from type II and type Ia supernovae and UV background radiation, with physical recipes identical to those applied in a previous study of Milky Way type galaxies. We find that a combination of feedback and the cosmic UV background results in the formation of galaxies with properties similar to the Local Group dwarf spheroidals, and that their effect is strongly moderated by the depth of the gravitational potential. Taking this into account, our models naturally reproduce the observed luminosities and metallicities. The final objects have halo masses between 2.3×10^8 and 1.1×10^9 M$_\odot$, mean velocity dispersions between 6.5 and 9.7 kms^{-1}, stellar masses ranging from 5×10^5 to 1.2×10^7 M$_\odot$, median metallicities between [Fe/H] $= -1.8$ and -1.1, and half-light radii of the order of 200 to 300 pc, all comparable with Local Group dwarf spheroidals. Our simulations also indicate that the dwarf spheroidal galaxies observed today lie near a halo mass threshold around 10^9 M$_\odot$, in agreement with stellar kinematic data, where supernova feedback not only suffices to completely expel the interstellar medium and leave the residual gas-free, but where the combination of feedback, UV radiation and self-shielding establishes a dichotomy of age distributions similar to that observed in the Milky Way and M31 satellites.

Key words: cosmology: theory – galaxies: dwarf – galaxies: formation – galaxies: evolution – Local Group – methods: N-body simulations.

1 INTRODUCTION

Dwarf spheroidal galaxies are amongst the smallest and faintest known galactic systems, and at first sight, should be easy to understand. Their name indicates a simple morphology, they possess low rotation, little or no interstellar gas and no active star formation. Their stellar masses range from less than 10^4 to a few times 10^7M$_\odot$, which even at the more luminous end, makes them comparable to the brightest globular clusters. However, whilst all observed dwarf spheroidal galaxies contain at least a fraction of very old stars (Grebel 1997), this is where the similarities with globular clusters end. Spectroscopic surveys of individual stars in several dwarf spheroidal galaxies of the Local Group (e.g. Battaglia et al. 2006) have revealed surprisingly complex star formation histories, sometimes over several Gyrs, and at least in one case in multiple bursts (Koch et al. 2006, 2008; Orban et al. 2008)

About two dozen dwarf spheroidal galaxies have so far been discovered as satellites of the Milky Way, while estimates using luminosity functions corrected for completeness and bias predict the total number of faint satellites to be an order of magnitude higher (Tollerud et al. 2008). The known dwarf spheroidal galaxies in the Local Group reside in a variety of environments. There are a few near both M31 and the Milky Way, with distances of ∼ 30 kpc and clearly within their hosts' dark matter haloes, as well as some remote objects like Cetus (Lewis et al. 2007) and Tucana (Castellani et al. 1996; Fraternali et al. 2009), which can be considered to have evolved in isolation.

It has been proposed for a long time (e.g. Faber & Lin 1983) and is now widely believed that the luminous component of dwarf spheroidal galaxies is not all there is to them. Their dynamics appear to be largely dark matter dominated, and measurements of stellar velocity dispersions (e.g. Koch et al. 2007; Walker et al. 2007; Mateo et al. 2008; Walker et al. 2009) indicate that they possess the highest mass-to-light ratios of any known galactic systems. Recent studies further suggest that despite the spread in luminosities, the total mass within the central 300 pc of each galaxy lies within a small range of around 10^7M$_\odot$ (Strigari et al. 2008).

[⋆] E-Mail: till@mpa-garching.mpg.de

Table 1. Overview of Numerical Simulation Results

Label	f_s	$M_\star$ $[10^6 M_\odot]$	M_g $[10^6 M_\odot]$	M_{tot} $[10^6 M_\odot]$	$M_{0.3}$ $[10^6 M_\odot]$	$M_{1.8}$ $[10^6 M_\odot]$	$M/L_{0.3}$ $[[M_\odot/L_\odot]_V]$	$M/L_{1.8}$ $[[M_\odot/L_\odot]_V]$	$r_{1/2}$ [pc]	Δ age [Gyrs]	[Fe/H]	σ $[kms^{-1}]$
Simulations including feedback, UV radiation and self-shielding [1]												
1	0.368	0.55	0.099	233.8	8.48	79.0	129	555	244	1.13	-1.78	6.55
2	0.422	0.96	0.005	348.8	9.71	103.6	100	409	303	1.15	-1.76	7.26
3	0.464	2.10	0.009	466.1	11.5	125.7	39	223	226	2.51	-1.52	7.54
4	0.500	2.68	0.006	585.3	13.2	147.3	39	209	246	1.78	-1.54	8.12
5	0.531	3.94	0.14	701.8	14.8	165.9	26	156	212	1.21	-1.46	8.47
6	0.559	9.02	0.010	809.3	16.3	185.7	13	81	164	3.10	-1.12	8.62
7	0.585	10.02	0.005	922.3	17.9	203.5	13	80	171	3.23	-1.17	9.08
8	0.608	12.20	0.011	1042	17.9	218.5	12	71	190	3.30	-1.15	9.62
9	0.630	12.26	0.012	1162	21.0	235.1	14	76	181	3.21	-1.14	9.71
Simulations including UV radiation but no supernova feedback [1] [3]												
10	0.422	18.77	0.82	318.4	14.5	113.3	8	28	118	3.75	-0.71	-
11	0.531	99.50	9.64	645.6	27.0	216.5	6	14	160	6.46	-0.21	-
Simulations including feedback, UV radiation but no shielding[1]												
12	0.368	0.53	0.002	233.2	8.40	79.2	129	571	271	1.09	-1.78	6.39
13	0.422	0.99	0.005	351.7	10.3	103.8	98	407	289	1.11	-1.70	7.43
14	0.464	1.95	0.015	463.8	11.6	126.0	48	240	254	1.11	-1.52	7.67
15	0.500	2.75	0.19	582.7	13.5	148.1	38	201	248	1.16	-1.48	8.31
16	0.531	4.19	0.20	697.8	15.5	168.6	27	152	208	1.17	-1.38	8.40
17	0.559	6.91	0.55	811.2	16.6	187.6	17	105	186	1.14	-1.27	8.45
18	0.585	6.69	0.38	939.4	18.0	202.6	18	113	180	1.21	-1.29	9.12
19	0.608	9.31	0.58	1051	18.1	217.9	15	89	197	1.18	-1.32	9.38
20	0.630	9.65	0.65	1179	18.9	235.2	16	93	196	1.12	-1.31	9.74
Simulations including feedback but no UV radiation[1]												
21	0.368	1.38	0.077	229.6	9.08	79.24	36	202	180	7.96	-1.09	6.28
22	0.422	2.58	0.10	344.2	11.8	105.3	27	143	180	7.60	-1.03	7.11
23	0.464	4.58	0.08	458.4	13.4	128.6	19	105	178	5.49	-1.08	7.39
24	0.500	5.72	0.11	576.2	15.4	150.3	18	99	165	5.25	-1.06	8.17
25	0.531	7.14	0.098	685.9	16.3	158.5	16	90	171	4.53	-1.08	8.33
26	0.559	9.26	0.086	798.5	17.4	186.9	14	81	157	2.59	-1.12	8.75
27	0.585	10.95	0.064	909.0	17.5	204.3	13	76	169	3.66	-1.05	9.17
28	0.630	13.70	0.003	1147	20.1	236.9	12	69	181	3.71	-1.09	10.0
Simulations including feedback, UV radiation and self-shielding[2]												
29	0.422	0.59	0.008	338.7	6.88	104.1	157	737	375	1.21	-1.78	7.20
30	0.630	7.35	0.066	1141	15.5	235.4	18	133	245	2.62	-1.11	9.50

Notes: Col. 2: Scale factor (length) of the initial conditions relative to Hayashi et al. (2003), Col. 3: Stellar mass, Col. 4: Gas mass within 1.8 kpc, Col. 5: Halo mass (M_{200}), Col. 6: Dark matter mass within 0.3 kpc, Col. 7: Dark matter mass within 1.8 kpc, Col. 8: Mass-to-light ratio (V-Band) within 0.3 kpc, Col. 9: Mass-to-light ratio (V-Band) within 1.8 kpc, Col. 10: Half light radius (projected), Col. 11: Formation time interval containing 90 % of $M_\star$, Col. 12: Median stellar iron abundance, Col. 13: RMS stellar velocity dispersion

[a] Initial number of particles: 1.7×10^5 gas, 8.7×10^5 dark matter.
[b] Initial Number of particles: 1.21×10^6 gas, 2.83×10^6 dark matter.
[c] Simulations terminated at $z = 0.68$

It is also worth pointing out that in galaxy formation, small size can breed complexity. Shallow potential wells make these systems susceptible to both internal and external effects, such as violent supernova feedback, photoionization and heating from the cosmic UV background, tidal interactions and ram-pressure stripping. All of these processes have the potential to shape the evolution of dwarf galaxies, and to leave their mark on the star formation history and the chemical abundances, as well as on the morphology and dynamics of the final objects. They may explain some of the peculiar properties of dwarf spheroidals, including their very high mass-to-light ratios, and may also be responsible for the observed scaling laws (e.g. Woo et al. 2008). In this sense, the evolution of dwarf spheroidal galaxies can be considered an extreme case, but at the same time, an extremely good laboratory for astrophysical and cosmological processes (Marlowe et al. 1995). While the sensitivity to many parameters represents a considerable challenge for simulations, the large number of dwarf galaxies in the Local Group, together with the availability of high quality observational data also provides an unusually high number of constraints. Revaz et al. (2009 in prep.) exploit this fact by studying a large number of idealised models with non-cosmological initial conditions, which they can tune to reproduce the observed relations.

The number of dwarf galaxies observed in the Local

Group continues to grow as new, 'ultra-faint' satellite galaxies are discovered (e.g. Martin et al. 2006; Chapman et al. 2008). Nevertheless, it is still much smaller than the total number of dark matter subhaloes found in high-resolution simulations of spiral galaxy haloes in the standard ΛCDM cosmology (e.g. Klypin et al. 1999; Moore 1999; Diemand et al. 2007; Springel et al. 2008). This has become known as the 'missing satellites problem'. However, this is only an apparent discrepancy. It is removed when one accounts for the fact that not all subhaloes contain stars. Two possible mechanisms that can produce a number of visible satellite galaxies similar to that observed are the following. Perhaps many haloes were able to form a few stars initially, but the baryonic components of all haloes below some critical mass were subsequently destroyed by supernova feedback (e.g. Dekel & Silk 1986; Ferrara & Tolstoy 2000). Alternatively (or perhaps additionally) photoionization may have prevented star formation in the smallest haloes (e.g. Efstathiou 1992; Somerville 2002; Simon & Geha 2007). As dwarf spheroidals are the faintest known galaxies, a detailed understanding of their evolution should eventually reveal the influences of these two effects.

Examples of earlier numerical studies of the formation of dwarf galaxies include simulations by Read et al. (2006), Mashchenko et al. (2008), Stinson et al. (2007, 2009) and Valcke et al. (2008). The latter two have investigated the collapse of gas clouds in dark matter haloes of constant mass. Both find evidence of prolonged and self-regulated star formation. However, while they do observe significant supernova-driven outflows, at a halo mass of $10^9 M_\odot$, Stinson et al. find better agreement with dwarf irregular galaxies. Read et al. performed simulations of the formation of the first baryonic building blocks in a cosmological volume at high redshift. They confirm the importance of supernova feedback and UV heating (assumed to begin at $z = 13$) for removing the gas from the smallest haloes. However, they do not follow the evolution of the surviving objects to the present day, terminating their simulations at $z = 10$. Mashchenko et al. have also performed cosmological simulations, albeit of noticeably more massive haloes, which they follow up to $z = 5$. They do not include UV radiation, and would require an additional mechanism to remove the gas from the galaxy, in order to form a system comparable to observed dwarf spheroidals. However, they find stellar properties in good agreement with the Fornax dwarf spheroidal, including globular clusters. They also predict that supernova feedback induces the formation of extended dark matter cores via gravitational resonance heating.

In this work, we model the formation and evolution of dwarf galaxies in fully cosmological, smoothed particle hydrodynamical (SPH) simulations. We simulate a cosmological volume with periodic boundary conditions, in which the haloes grow from small density perturbations imposed at high redshift. Our initial conditions are chosen to reproduce galaxies of halo masses similar to the ones inferred for the Local Group dwarf spheroidals. Because we follow the evolution to $z = 0$, and because we include the environment in a consistent way, our mass-resolution is somewhat lower compared with simulations of isolated haloes, or simulations which end at high redshift. However, the cosmological nature of our simulation allows us to simultaneously follow the growth of the dark matter halo, and the evolution of the dissipative component. The full time-evolution also reveals the effect of the UV background, and lets us directly compare present-day properties to the observations. Our numerical model includes cooling, star formation, chemical enrichment and feedback, and we allow for exchange of material with the intergalactic medium. We also include cosmological effects such as reionization. We use the same code, and with a few notable exceptions owing to the different physical effects that play a role in the two regimes, we use the same physics model and basic parameters as those employed by Scannapieco et al. (2008) in their study of the formation of Milky Way type disk galaxies, some 10^4 times larger in terms of stellar mass than the dwarf galaxies we consider here. We do not study local environmental effects, which may play a role for the closest companion satellite galaxies to the Milky Way. The main questions that we will address are how it is possible that systems of such low luminosity and seemingly similar total masses undergo such complex and diverse star formation histories, why dwarf spheroidal galaxies have such high mass-to-light ratios, why they appear to follow certain scaling laws, and if their formation and evolution in a cosmological constant dominated Cold Dark Matter (ΛCDM) universe can be explained by a consistent physical model. In Section 2, we present the computational methods which we have used and our choice of initial conditions. Section 3 follows with a presentation of the results of our simulations in broad terms, while we pay closer attention to the relevance of individual physical processes, particularly supernova feedback and UV radiation, in Section 4. In Section 5, we focus on the observed scaling laws, and present the dependence of our results on model parameters. We conclude with a summary where we discuss the achievements and shortcomings of the simulations in Section 6, and look forward to our future work.

2 METHODS

The simulations presented here have been performed using the Tree-PM code GADGET-3 (Springel 2005; Springel et al. 2008), which includes gravity and smoothed particle hydrodynamics. As an extension, metal-dependent cooling, star formation, chemical enrichment and energy injection from type II and type Ia supernovae have been implemented in the multiphase gas model of Scannapieco et al. (2005, 2006). This model has previously been used to study the effect of feedback on galaxy evolution in general terms (Scannapieco et al. 2006) and the formation of disk galaxies in particular (Scannapieco et al. 2008, 2009). In addition, some of our simulations contain an approximative treatment of self-shielding and low temperature cooling, which were not included in the previous model. In this section, we explain the most important characteristics of our model.

2.1 Cooling

Above the hydrogen ionization temperature of 10^4 K, our gas cooling model is based on metal-dependent cooling functions of Sutherland & Dopita (1993). When we include cooling below 10^4 K, we use the extension of Maio et al. (2007). The adopted cooling function $\lambda(T)$, normalized to $n_H = 1$

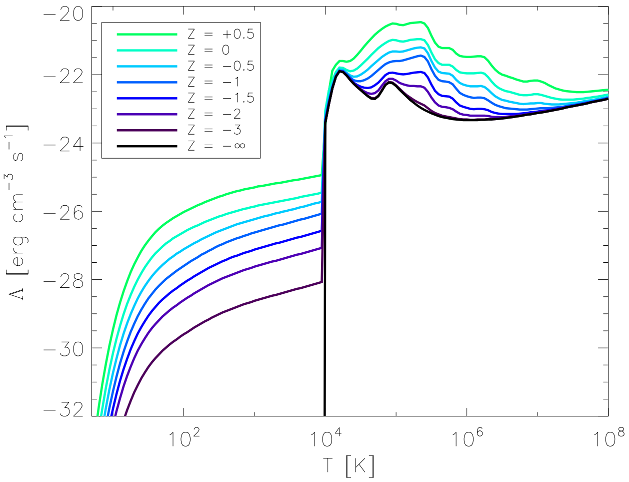

Figure 1. Normalized net cooling rate $\left[\lambda/n_H^2\right]$, adopted from Sutherland & Dopita for temperatures above 10^4 K, and Maio et al. for lower temperatures. The metal-dependency is expressed in solar units, assuming $\mathrm{Z}_\odot = 0.02$.

cm^{-3}, is shown in Figure 1 for eight different metallicities. In our models, the gas density is typically below $n_H = 3 \times 10^3$ cm^{-3}. Consequentially, we do not consider the effect of rotational excitations, and the resulting linear density dependence in the high density limit (Dalgarno & McCray 1972).

The ionization states of H, He, and the electron number density are computed analytically, following the model of Katz et al. (1996). Compton cooling, which is not included in Figure 1, is the main coolant at high redshift, and implemented as a function of the free electron density as well as the temperature difference between the gas and the evolving CMB temperature.

The effect of the UV background on the net cooling function, and on the temperature evolution of the gas, is described in Section 2.4, and depends on the abundance of the different species of H and He. We note that the metal-dependent cooling functions of Sutherland & Dopita (1993) assume collisional ionization equilibrium. As Wiersma et al. (2009) have recently shown, the presence of an ionizing radiation background can significantly decrease the cooling efficiently compared to collisional equilibrium in optically thin gas. This effect is in addition to the direct UV heating, and is neglected in our model. However, because the galaxies in this study form before reionization (see Section 3), and because the current implementation already predicts inefficient cooling of the optically thin gas after the UV background is switched on (see Section 4.2), we expect that it would not qualitatively alter our results.

Below $10^4 K$, the cooling rate is a strong function of metallicity, which Maio et al. (2007) have calibrated to different iron abundances. In section 4.4, we investigate the significance of low temperature cooling in our simulations. In general, the difference is small, except for objects with virial temperatures significantly below 10^4 K.

2.2 Star Formation

Star formation is implemented so that gas particles can spawn, or be converted into, star particles, subject to certain conditions. We require the gas particle to be in a region of convergent flow. In addition, we impose a physical density threshold ρ_c on the local gas density. The existence of a threshold for star formation is motivated by observations (e.g. Kennicutt 1989, 1998). Calculations by Quirk (1972) as well as numerical simulations, e.g. by Katz et al. (1996); Springel & Hernquist (2003); Bush et al. (2008) and others have shown that the observed Kennicutt-Schmidt relation can be reproduced imposing a volume density threshold, even though slightly different values are derived. Recently, Koyama & Ostriker (2009) demonstrated with high-resolution simulations of the turbulent interstellar medium that the star formation rate depends only weakly on the choice of ρ_c, and we adopt the value of $\rho_c = 7 \times 10^{-26}\mathrm{gcm}^{-3}$, that was used in Scannapieco et al. (2006). We also impose a threshold of $\rho_\mathrm{g}/\overline{\rho_\mathrm{g}} \geqslant 57.7$ on the local gas overdensity (where $\overline{\rho_\mathrm{g}}$ is the global mean density). This corresponds to a mean enclosed overdensity which is the minimum overdensity of a spherical, r^{-2} perturbation for gravitational collapse, and ensures that even at high redshift, star formation takes place only in virialised regions (Katz et al. 1996). Subject to these constraints, the local star formation efficiency is regulated by a single efficiency parameter $c_\star$, so that the star formation rate is given by

$$\frac{d\rho_\star}{dt} = c_\star \frac{\rho_g}{t_\mathrm{dyn}}$$

where t_dyn is the local gas dynamical time. The creation of an individual stellar particle of mass $m_\star$ from a gas particle of mass m_g during the time interval Δt is stochastic, with the probability given by

$$p_\star = \frac{m_g}{m_\star}\left(1 - exp\left(-c_\star \frac{\Delta t}{t_\mathrm{dyn}}\right)\right).$$

In most of our simulations, we adopt a choice of $c_\star = 0.05$. We study the effect of different values in Section 5.3. Each star particle thus produced contains a single stellar population, whose metallicity is inherited from the parent gas particle. For simplicity, we assume a Salpeter initial mass function (Salpeter 1955). We calculate the luminosities at any given time using the stellar evolution model of Bruzual & Charlot (2003).

2.3 Multiphase Interstellar Medium and Feedback

For each star particle, we determine the rate as well as the yields of supernovae type II and type Ia. Chemical yields are calculated separately for both types, following Woosley & Weaver (1995) and Thielemann et al. (1993) respectively. Supernovae type II are assumed to be instantaneous, while for supernovae type Ia, we assume a uniform delay time distribution with given minimum and maximum delay times, as discussed in Section 5.4. We assume a constant energy production of 10^{51} ergs per supernova, which is released into the interstellar medium (ISM) as purely thermal energy.

The multiphase characteristic of the ISM, in which components of a wide range in temperature and density coexist, is lost in simple SPH models, where the smoothing kernel is a function of position only. This leads to an overestimation of the density in diffuse clouds neighbouring high density regions, and results in an underestimation of their cooling times, artificially increasing the star formation rate. It also means that feedback from supernovae is released primarily to the gas in star forming regions, where the densities are normally so high that the energy is lost immediately via radiative cooling. As a result, outflows and self-regulation of star formation are severely suppressed, and metals remain confined (Katz 1992; Marri & White 2003).

Most simulators fix the second problem by switching off cooling in the reheated particles for some time (e.g. Thacker & Crouchman 2000; Governato et al. 2007), or by giving them a kick of arbitrarily specified amplitudes (e.g. Navarro & White 1994; Dalla Vecchia & Schaye 2008). The multiphase scheme for the interstellar medium of Scannapieco et al. (2006), addresses the problems at a fundamental level. It allows an overlap of diffuse and dense gaseous components by considering as neighbours in the smoothing kernel only gas particles with similar thermodynamic properties. Specifically, particles i and j are mutually excluded as neighbours if the ratio of their entropic functions $A(s)_{ij}$ exceeds a certain threshold and their pairwise-averaged velocity divergence multiplied by their mutual separationfalls below the local sound speed, which avoids the decoupling of shock-waves.

However, this approach introduces some additional freedom in determining how the energy and metals released by supernovae are shared between the gas particles of the multiphase medium, which in our simulations each receive half of the total energy. In the dwarf galaxies we have simulated, most of the ejecta given to gas particles in the hot and diffuse phase eventually escape from the system, leaving mostly those that go to the cold phase to be included in subsequent generations of stars. Thus, increasing the fraction of metals given to the cold phase increases the final metallicity for a given stellar mass, whereas a high fraction of metals given to the hot phase creates strongly metal-enhanced winds. To some extent, we can use the observed metallicity-luminosity relation of dwarf spheroidals, shown in Figure 11, in order to calibrate this parameter. Because it effects all elements in the same way, the remaining degeneracy with the supernova Ia lifetimes can be partially broken by also considering the [Ca/Fe] ratios. We find relatively good agreement if 25% of the metals and energy are injected to the cold phase, and we use this value for all the simulations presented in this work.

2.4 UV background

Quasar spectra indicate that the universe has been fully ionised from about redshift $z = 6$ (Fan et al. 2002). This has prompted us to include UV background radiation in our models, and we discuss its influence in Section 4.2. The question of whether dwarf galaxies survive the cosmic reionization epoch has been an intense area of study (e.g. Kitayama et al. 2002; Susa & Umemura 2004; Hoeft et al. 2006, 2008). In hydrodynamical simulations, Hoeft et al. (2008) find that UV heating reduces the baryonic fraction in galaxies below a characteristic total mass, $6 \times 10^9 \mathrm{M}_\odot$. However, Grebel & Gallagher (2004) found no clear signature of a widespread impact from reionization in their analysis of age distributions of nearby dwarf galaxies. In those simulations where the UV background is included, we have modified the cooling function for partially ionized gas by a heating term. Apart from tests where we have decreased the UV intensity, the intensity evolution of the UV background follows that of Haardt & Madau (1996).

2.5 Initial Conditions

All simulations are performed in the context of a ΛCDM cosmology, with $\Omega_\Lambda = 0.7$ and $\Omega_\mathrm{m} = 0.3$. We use a set of initial conditions based on pure dark matter simulations of isolated haloes by Hayashi et al. (2003). The halo on which our simulations are based (labeled D1 by Hayashi et al.) was selected from their set of dwarf haloes in order to yield an object whose high redshift progenitors fill a compact region in space, enabling us to limit the high resolution region to a small fraction of the total volume, whose (unscaled) side length is 35.25 h^{-1} Mpc. The resimulations start at redshift $z_i = 74$ with density fluctuations corresponding to a present value of $\sigma_8 = 0.9$ in the unscaled initial conditions. To the dark matter, gas particles were added at a rate of $\Omega_\mathrm{b} = 0.04$ and $\Omega_\mathrm{DM} = 0.26$. As indicated in Table 1, we have scaled the initial conditions at constant density, to give final halo masses between 2.33×10^8 and 1.18×10^9 $h^{-1}\mathrm{M}_\odot$, but identical formation redshift and (scaled) assembly histories for all our objects. This causes an effective change of the normalisation of the power spectrum between the simulations, but as Colin et al. (2004) have shown, due to the early formation of dwarf haloes and the flatness of the linear fluctuation amplitude in this mass regime, the influence on the evolution of individual haloes is expected to be insignificant compared to the scatter between objects.

As described in Section 2.6, we have also performed simulations of varying particle numbers (up to 2.83×10^6 for dark matter and 1.21×10^6 for gas). The gravitational softenings for each particle type were fixed to 1/10th of the respective mean interparticle separation in comoving coordinates in the initial conditions and limited, in physical coordinates, to ∼ 1/5th of the mean separation within the collapsed haloes. This allowed a spatial resolution typically below 100 pc (depending on the scale and the number of particles). Haloes were identified using a friends-of-friends method with a linking length of 0.2. In each case, over a hundred small haloes with 32 particles or more were formed in the simulated volume, and depending on the choice of parameters of the baryonic physics model, several of them formed stars. However, in each case we limit our analysis to the most massive one, for which the effective resolution is highest. We have made tests to confirm the scale-free behaviour of the pure dark matter simulations. We find that in all cases, the dark matter profiles are well-fitted by a Navarro, Frenk and White (NFW) model, down to the resolution limit. Note that all our simulations have the same assembly history, apart from resolution effects. This means that we cannot say anything about the scatter in properties expected among similar mass haloes. On the other hand, differences between our various simulations must therefore be due entirely to differences in the assumed physics or the numerical parameters. Cosmic variance plays no role.

2.6 Effects of Resolution

The hydrodynamical model, and the recipies for feedback and star formation may also be influenced by resolution effects. Scannapieco et al. (2006) have tested the model for numerical convergence. Since we extend their model to a new mass range, we have performed additional tests. Simulations 1-28, summarized in Table 1, are run with a constant number of 8.7×10^5 dark matter particles, 1.7×10^5 of which are in the high resolution Lagrangian volume that also contains 1.7×10^5 gas particles. The corresponding particle masses range from $6.6 \times 10^3 \mathrm{M}_\odot$ and $1.2 \times 10^3 \mathrm{M}_\odot$ in simulation 1, to $3.3 \times 10^4 \mathrm{M}_\odot$ and $5.8 \times 10^3 \mathrm{M}_\odot$ in simulation 9, for dark matter and gas particles, respectively. The number of stellar particles varies, depending on star formation rate, and the stellar particle masses range between $5.4 \times 10^2 \mathrm{M}_\odot$ in simulation 1 and $2.7 \times 10^3 \mathrm{M}_\odot$ in simulation 9. Wherever we have changed the other parameters of the model, we have kept the resolution fixed. We have also performed two simulations, 29 and 30, with a mass resolution increased by a factor of eight compared to simulations 2 and 9, respectively, while all other parameters were kept constant. The results are shown in the bottom rows of Table 1. While the respective total masses of the systems are constant to within a few percent, a statement of the fact that the gravitational part of the force calculations is largely resolution-independent, and that the coupling of the dark matter to the baryons in our simulations is small, the total stellar mass produced in both cases decreases by $\sim 40\%$. With increased resolution, star formation begins slightly earlier and at lower halo masses, resulting in quicker heating and outflows of the gas. However, this difference is small compared to the influence of physical parameters, such as total mass. The simulations at different resolutions also show similar properties with respect to the response to the UV background, the self-shielding threshold and the metal-enrichment. The results remain consistent with global scaling relations, as illustrated in Figures 11 and 13, where we have included the high resolution results of simulations 29 and 30, together with the results of simulations 1-9.

3 FORMATION AND EVOLUTION

We find that the evolution of the dwarf galaxies that we simulate is strongly affected both by supernova feedback and by the UV background radiation. It is the combination of these two effects that shapes the evolution of the galaxy. We begin this section by showing the evolution of a typical dwarf galaxy up to the present time, including all the different effects that play a role, but focusing on the global picture. We then try to disentangle the effects of feedback and UV radiation, and look in more detail at how they each influence the evolution in Section 4.

3.1 Time Evolution

Figure 2 illustrates different stages in the evolution of a proto-galaxy (labeled simulation 16 in Table 1) together with its environment. The top row shows the position of dark matter, gas and star particles. The scale of the panels is kept constant in physical coordinates with a side length of 20 kpc, hence the volume displayed shrinks in terms of comoving coordinates and the view zooms in on the central galaxy as the redshift decreases from left to right. In the first two columns, the filamentary structure of the environment is still recognisable, together with a number of smaller haloes that have accumulated gas, but not yet begun star formation. The bottom row shows the distribution of gas particles on the density-temperature plane, both within and outside of the most massive halo.

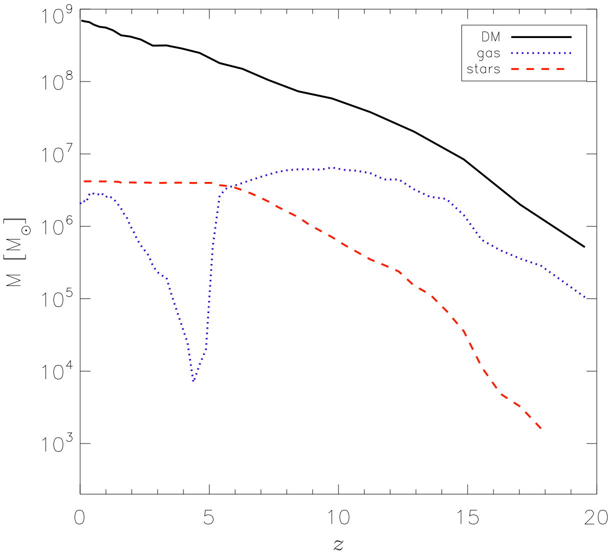

Figure 3. Evolution of the bound dark matter mass (solid black), gas mass (dotted blue) and stellar mass (dashed red) as function of redshift for simulation 16, the same simulation that is shown in Figure 2 in several snapshots. The simulation includes cooling, star formation, supernova feedback and a cosmic UV background, but no self-shielding. It reaches a virial mass of $\sim 7 \times 10^8$ M$_\odot$, and a stellar mass of $\sim 4 \times 10^6 \mathrm{M}_\odot$ at $z = 0$. Other properties are summarised in Table 1.

As the halo forms, gas begins to fall in, contracts and gets heated. At a temperature of 10^4 K, radiative cooling becomes so efficient that the gas can contract essentially isothermally, until the central density reaches the threshold for star formation, as described in Section 2.2. At $z = 12.3$, which corresponds to the leftmost column of Figure 2, the first stars have already formed in the central object, and supernovae of type II have started heating the gas, already pushing some of it out. This is visible also in the bottom row of Figure 2, where the gas particles that start appearing to the right of 10^4 K, which indicates that they have been heated by supernovae, are no longer bound to the halo.

The total masses of the three components; dark matter, gas and stars identified as belonging to the halo by a friends-of-friends algorithm, are shown as a function of time in Figure 3. Star formation in the galaxy continues for about one Gyr, as more gas gets accreted and cools, whilst supernovae of both type II and type Ia continue to expel the interstellar medium. Ejection and heating balance accretion and cooling at $z = 9$, and the star formation rate peaks at $z = 8$. By redshift $z = 6$, the star formation rate has already decreased by a factor of two from its peak value of $3 \times 10^{-1} \mathrm{M}_\odot$ yr^{-1} due to feedback.

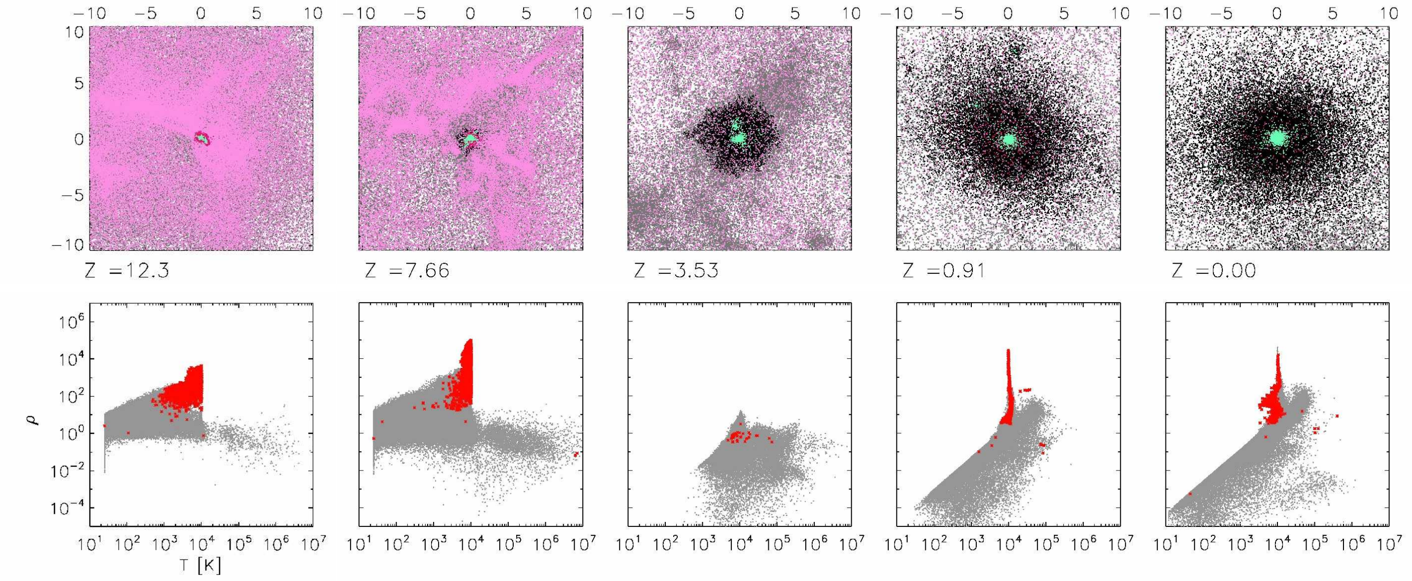

Figure 2. Top row: Spatial distribution of particles of different types at different redshifts of simulation 16 in Table 1. Dark matter particles are shown in black (or grey), gas particles in red (or purple), depending on whether they are bound to the object in the centre, or whether they are part of other haloes or the intergalactic medium. Star particles are shown in green. Bottom row: Temperature and density of gas particles. Red dots indicate gas that is bound to the central halo, while grey dots are for particles in all other parts of the simulated volume. Both supernova feedback and UV radiation are included in this simulation, which has a final halo mass of $\sim 7 \times 10^8 \mathrm{M}_\odot$. It can be seen that the central halo is almost gas-free at redshift $z = 3.5$, due to the combined effect of feedback and the UV background. Feedback heats the gas and blows some of it out during the early stages of the evolution. After redshift $z = 6$, UV radiation heats the remaining gas above the haloes virial temperature, quickly removing it from the halo, and it also heats the intergalactic medium. Some gas falls back to the main halo at later times, but does not lead to significant amounts of star formation. Smaller haloes without star formation, and hence not subject to feedback, also lose their gas due to the UV radiation.

At $z = 6$, the UV background suddenly switches on. In this particular model, it is sufficient to heat the remaining gas above the virial temperature of the halo in a very short time, resulting in its expulsion, and a sharp end to star formation. Some gas falls back at a later stage, but does not reach sufficient density for significant star formation.

It can also be seen in Figure 3 that the dark matter halo in this simulation continues to grow over time through accretion and minor mergers. It is worth noting that throughout the period of star formation, from the onset around redshift $z = 16$ to the end shortly after redshift $z = 6$, the halo mass is several times smaller than the final value, which might be observed today. This behaviour is common to all of our simulations, independent of the baryonic physics. It contributes to the high efficiency of the winds in our models. It also suggests that the impact that supernova feedback might have had during the history of a particular dwarf galaxy not only depends on its 'mass' as it is presently observed, but also on the co-evolution of its star formation and the assembly of its halo at earlier times. This fact is taken into account explicitly in semi-analytic models like that of Ferrara & Tolstoy (2000), but it is overlooked in non-cosmological simulations that assume collapse in a static potential.

In our simulations, the halo continues to grow unperturbed up to $z = 0$. This is not necessarily true for haloes of satellite galaxies, which may have experienced truncation upon infall (Nagai & Kravtsov 2005). However, at least according to our models, it is likely that star formation would have finished before a typical infall redshift of $z \sim 1$ or below (Li & Helmi 2008). While we therefore do not expect environmental effects to significantly alter the stellar population, they may further skew the correspondence between observed halo masses today, and gravitational potential in place at the epoch of star formation. We also have to assume that the late infall of gas, leaving in some cases a small amount of gas at $z = 0$, which would be in disagreement with observations, is prevented in the Local Group environment.

4 THE ROLE OF PHYSICAL PROCESSES

As we have seen, feedback from supernovae is sufficient to expel gas from the shallow potential wells of forming dwarf-galaxies, and it is responsible for regulating star formation at least up to redshift $z = 6$. In order to investigate the relative importance of feedback and UV heating, and to disentangle their respective contributions over time, we have performed test simulations where only one of the two processes is included.

Figure 4 illustrates two such 'incomplete' scenarios. We show the evolution of dark matter, gas and stellar mass, for simulation 25, where feedback is the *only* source of thermal energy, and for simulation 11, where UV radiation is included, but stellar feedback is ignored. They can be compared with our reference simulation 16 in Figure 3, where the combined effect of supernova feedback and UV background radiation are shown. All three simulations have identical ini-

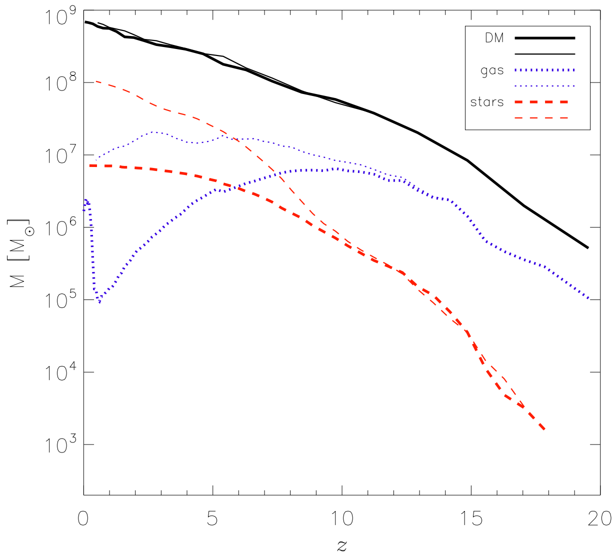

Figure 4. Evolution of the dark matter mass (solid black), gas mass (dotted blue) and stellar mass (dashed red) as functions of redshift, for simulations 25 and 11. Initial conditions and the final dark-matter mass of $\sim 7 \times 10^8 M_\odot$ are identical to those of simulation 16, shown in Figure 3, but the evolution is different. The thick lines show the evolution of simulation 25, where feedback is the only source of heating, whereas the thin lines are for simulation 11, that includes UV radiation from redshift $z = 6$ but no feedback. In the first case, feedback alone is sufficient to remove most of the gas, but more slowly compared to Figure 3. In the case of simulation 11, in the absence of feedback, the decline in the gas mass is solely due to consumption and conversion to stars. Furthermore, without feedback, the UV background present from $z = 6$ has almost no effect on the gas mass or the star formation rate. The resulting stellar masses are vastly different: $7 \times 10^6 M_\odot$ without UV for simulation 25, and $\sim 10^8 M_\odot$ for simulation 11 without feedback.

tial conditions and numerical resolution. While the growth of the dark matter mass appears unaffected by the baryonic physics, the dashed and dotted lines, which indicate the stellar and gas mass, respectively, show large differences. The outflow induced by feedback in simulation 25 causes the thick dotted line representing the gas mass in Figure 4 to peak at about $z = 9$ and decline thereafter, similar to Figure 3. The star formation rate (not shown) also declines and the thick dashed line, representing the total stellar mass, increases ever more slowly, reaching $7 \times 10^6 M_\odot$ at redshift $z = 0$. In contrast, the thin dotted line in Figure 4, which represents the gas mass without feedback, shows no decline at high redshift. The total baryon fraction of the halo stays constant at around 1/6th, indicating that the late decline of the gas mass is due solely to consumption by star formation. It is worth reiterating that this simulation includes the full UV background (see Section 4.2), without self-shielding (see Section 4.3). However, contrary to the results of Figure 3, we find that when thermal feedback is ignored, the UV radiation has no effect either. The gas density is so high that the gas can cool fast enough to balance any heating due to the cosmic UV background.

4.1 The Importance of Feedback

In summary, we find that feedback alone can blow out all the remaining gas before redshift $z = 0$ even in the absence of photoelectric heating, albeit at a much slower rate, resulting in a larger number of intermediate age stars. Even in this case, only between 3% and 6% of the total amount of gas ever bound to the halo gets turned into stars, depending on the mass of the object. Most of the gas still escapes to the intergalactic medium, enriching it with metals.

In simulations without thermal feedback (simulations 10 and 11 in Table 1, thin lines in Figure 4), the picture is drastically different. Not only is the star formation more efficient during the early stages, the interstellar gas also becomes so dense that all effects of the UV background radiation discussed in Section 4.2 are eliminated due to very efficient cooling. The result is a system of large stellar mass (up to $10^8 M_\odot$ in the case of simulation 11, compared to $4 \times 10^6 M_\odot$ for the same initial conditions run with feedback), low mass-to-light ratio, high metallicity, an abundance of young stars, and a high gas content. All these properties are incompatible with observations of Local Group dwarf spheroidals.

We conclude that feedback is necessary to shut down star formation in those haloes massive and dense enough to cool and begin forming stars. Under the assumption, supported by observations (e.g. Lewis et al. 2007; Fraternali et al. 2009), that at least some of the local Group dwarf spheroidals have evolved in isolation, these results suggest that supernova feedback is the key factor in determining their stellar evolution.

4.2 The Influence of the UV Background

To further elucidate the influence of the UV radiation, in Figure 5, we show the evolution of a system that includes feedback but no UV radiation (simulation 25 in Table 1), a simulation otherwise identical to our reference simulation 16 described in Section 3.1, which is shown in Figures 2 and 3. The most obvious difference to note when comparing the two sets of figures is in the low density regions of the intergalactic medium not part of our main halo, where heating by the UV background is most effective.

We find that all haloes that are not massive enough to accrete sufficient gas to form stars before $z = 6$ subsequently lose their gas when the effects of photoelectric heating are included. One consequence of this is that while the main halo grows through accretion of smaller haloes, these minor mergers are essentially gas-free and do not trigger renewed star formation. It also supports the idea that reionization establishes a lower mass threshold for dwarf galaxy haloes, and so provides part of the solution to the 'missing satellites problem'. However, we do not observe star formation in these haloes, even when UV radiation is ignored, most likely due to inefficient cooling as a result of insufficient resolution.

For those objects we consider as the progenitors of dwarf galaxies listed in Table 1, i.e. those massive enough to acquire dense, star-forming gas at high redshift, we have already shown that the UV background alone is not sufficient to shut off star formation at $z = 6$. Feedback is required in order to make the gas diffuse and to reduce its radia-

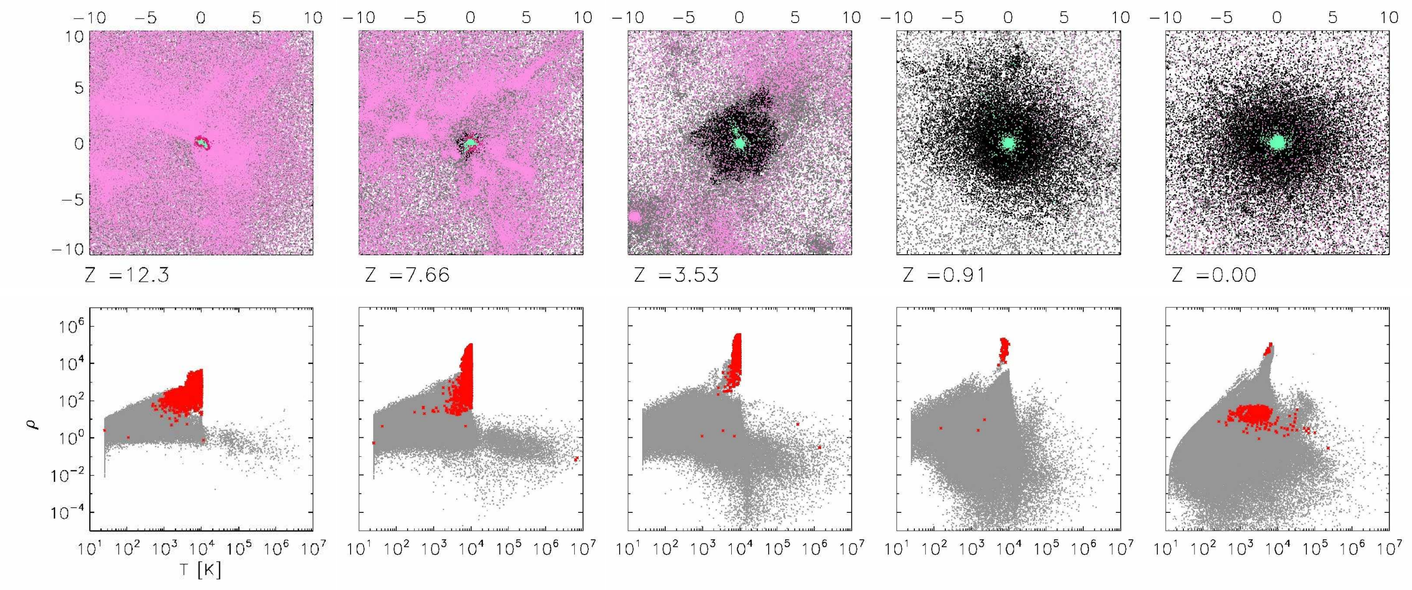

Figure 5. Top row: Spatial distribution of particles of different types at different redshifts of simulation 25. Dark matter particles are shown in black (or grey), gas particles in red (or purple), depending on whether they are bound to the object in the centre, or whether they are part of other haloes or the intergalactic medium. Star particles are shown in green. Bottom row: Temperature and density of gas particles. Red dots indicate gas that is bound to the central halo, while grey dots are for particles in all other parts of the simulated volume. Simulation 25, also shown in Figure 4 (thick lines), has initial conditions identical to the one shown in Figure 2, but contains no UV radiation. It reaches a final halo mass of $\sim 7 \times 10^8$. While the system still looses almost all its gas, this happens more slowly compared to the case with UV radiation, and the stellar mass continues to grow beyond redshift $z = 6$. The most noticeable difference, however, is in the smaller haloes (10^6 $M_\odot$ or less), which did not form stars early on, and which would now be able to retain their gas.

tive cooling efficiency. However, when this requirement is met, the UV background radiation has a strong influence on the star formation timescale. While the difference in total stellar mass in a given dark matter halo varies from 30 % for the largest system to a factor of three for the smallest system we have studied, this alone may not be enough to be discriminatory when comparing mass-to-light ratios with observations. However, a substantial difference is also found in the age and metallicity distributions. When star formation continues beyond reionization, many intermediate age stars with high metallicities are formed, and, as can be seen in Table 1, this causes the median metallicity to saturate around [Fe/H] $= -1.1$ when the UV background is ignored. Moreover, while properties such as the total stellar mass and metallicity also depend on the initial mass and (less strongly) on other parameters of the model (see Section 5), the age distribution of the stars does not. In all cases with UV radiation, the termination of star formation at $z = 6$ results in a narrow age distribution, as can be seen in Figure 6, while in all cases without the UV background, there is a pronounced intermediate-age tail. This is significant, because there appear to be examples of both types of galaxies in the Local Group (Grebel & Gallagher 2004). We have tested the dependence on the overall UV intensity, and found qualitatively similar results when we decreased it by up to a factor of 10 from the Haardt & Madau (1996) level. Furthermore, while there may be local variations in the UV background, particularly at higher redshift and from sources other than quasars (e.g. Ciardi et al. 2003), the mean free path of UV photons in the intergalactic medium is on the order of tens of Mpc (Bolton et al. 2004). This seems to rule out the possibility that the observed variation in star formation histories within the Local Group dwarf spheroidals can be attributed solely to small-scale variations of the UV background radiation level originating from quasars at large distances.

4.3 The Effect of Self-Shielding

We have also performed simulations where we approximate the effects of self-shielding of the dense interstellar medium against the UV background. While we do not include radiative transfer in these simulations, we use a threshold on the density of neutral hydrogen (HI) gas of $n_{\rm HI} = 1.4 \times 10^{-2}{\rm cm}^{-3}$, following the results of Tajiri & Umemura (1998). Including this effect leads to an interesting dichotomy. At the more massive end, as shown in the bottom row of Figure 7, the evolution in the central object proceeds almost as in the case with no UV background, while at the low mass end, as shown in the top row of the same figure, the evolution is similar to the case with UV heating but no shielding.

Figure 8 shows the star formation rates over time for a total of six simulations of two different halo masses. Simulations 2 and 7 which include shielding, as discussed above, are compared to two sets of equal mass-mass counterparts: Simulations 13 and 18 which have a UV background but no shielding, and simulations 22 and 27, which do not include UV radiation. The evolution of each triplet of a given mass proceeds identically up to redshift $z = 6$. Subsequently, the

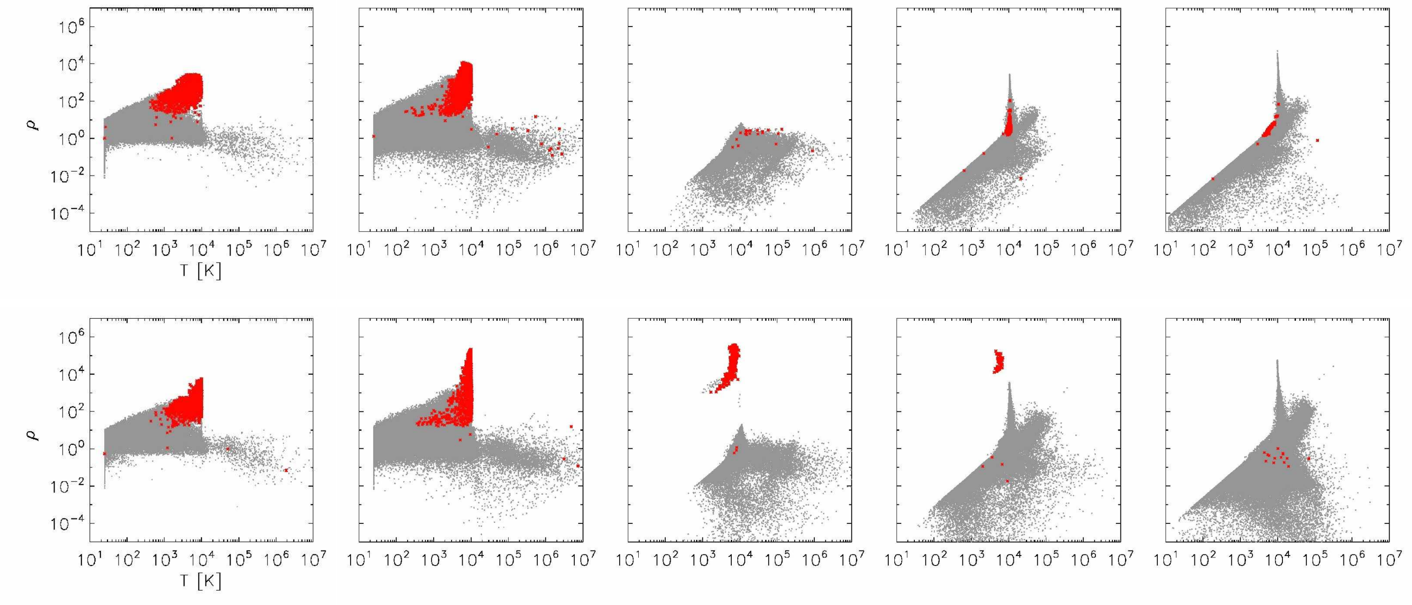

Figure 7. Temperature and density of gas particles. Red dots indicate gas that is bound to the central halo, while grey dots are for particles in all other parts of the simulated volumes. Results from two simulations of different mass illustrate the effect of self-shielding. Simulation 2, shown on top, has a final halo mass of $3.5\times10^{8}\mathrm{M}_{\odot}$, while simulation 7, shown below, reaches $9.2\times10^{8}\mathrm{M}_{\odot}$. Both simulations include supernova feedback and UV radiation, similar to those shown in Figure 2. At redshift $z = 7.6$, prior to reionization, the higher mass simulation has been able to keep a larger amount of dense interstellar gas in the centre, whereas feedback has caused the gas in the lower mass galaxy to be more diffuse. At redshift 3.5, the gas in the lower mass galaxy has been lost, while the higher mass galaxy has kept its high density gas, allowing it to form stars up to redshift $z = 1$. In both cases, grey dots, associated with the IGM and smaller haloes, are distributed similarly to the case with UV heating but no shielding in Figure 2, indicating that self-shielding is not efficient in these low density environments.

presence of the UV background quenches star formation in both simulations without shielding, while the two simulations without UV radiation both see a gradual decline in their star formation rate, solely due to feedback. However, when shielding is included, it has no effect in the low-mass case, where the star-formation rate shows a sharp decrease, similar to the unshielded case. In contrast, in the high-mass case, the star formation rate with shielding closely follows that of the corresponding simulation without UV radiation.

The age distributions shown in Figure 9 reflect this behaviour. Systems with lower mass only have small age spreads resulting from a single burst, comparable with the results without shielding shown in Figure 6 (matching colours indicate equal masses). Higher mass objects possess intermediate age tails, similar to the result without a UV background.

Again, we find that while it is the response of the interstellar medium to the UV radiation that ultimately splits the two scenarios, it is the effect of feedback prior to reionization that is at the root of this dichotomy. In the low-mass case, feedback dilutes the gas more efficiently prior to reionization, and thereby prevents it from self-shielding. In the high-mass case, the gas in the centre remains dense enough to become self-shielding and to prevent a blow-away.

While the approximation of self-shielding is very crude, and should be confirmed by more detailed analysis with full radiative transfer, it is interesting that the critical gas density that determines whether galaxies form stars after reionization appears to lie just at the right level to allow the formation of both kinds of dwarf spheroidal galaxies in simulations which include supernova feedback. On the basis of these arguments, it appears that the inclusion of cosmic reionization and a UV background with the possibility of self-shielding is the physically correct assumption. In the subsequent analysis, we continue to use the Haardt & Madau (1996) model, together with the Tajiri & Umemura (1998) approximation for self-shielding. We note, however, that the environment in which our galaxies form is different to that of the Local Group. This may play an additional role in the star formation history. Possible environmental effects include not only a local variation in the UV background, but also other mechanisms for removing gas, or reducing its density in satellite galaxies. While the removal of gas, by ram pressure stripping, for example, could halt star formation directly, our results indicate that an indirect mechanism might be just as efficient, if it makes the gas susceptible to evaporation after $z = 6$. That such environmental effects play a role is supported by the observation that dwarf spheroidals close to the centre of the Milky Way tend to have fewer intermediate age stars than those further out, although this trend is less clear for the M31-satellites (Grebel 1997).

4.4 The Role of Low Temperature Cooling

As described in Section 2.1, we have performed simulations with and without metal and molecular cooling below 10^{4} K. Bromm & Clarke (2002) found in their simulations

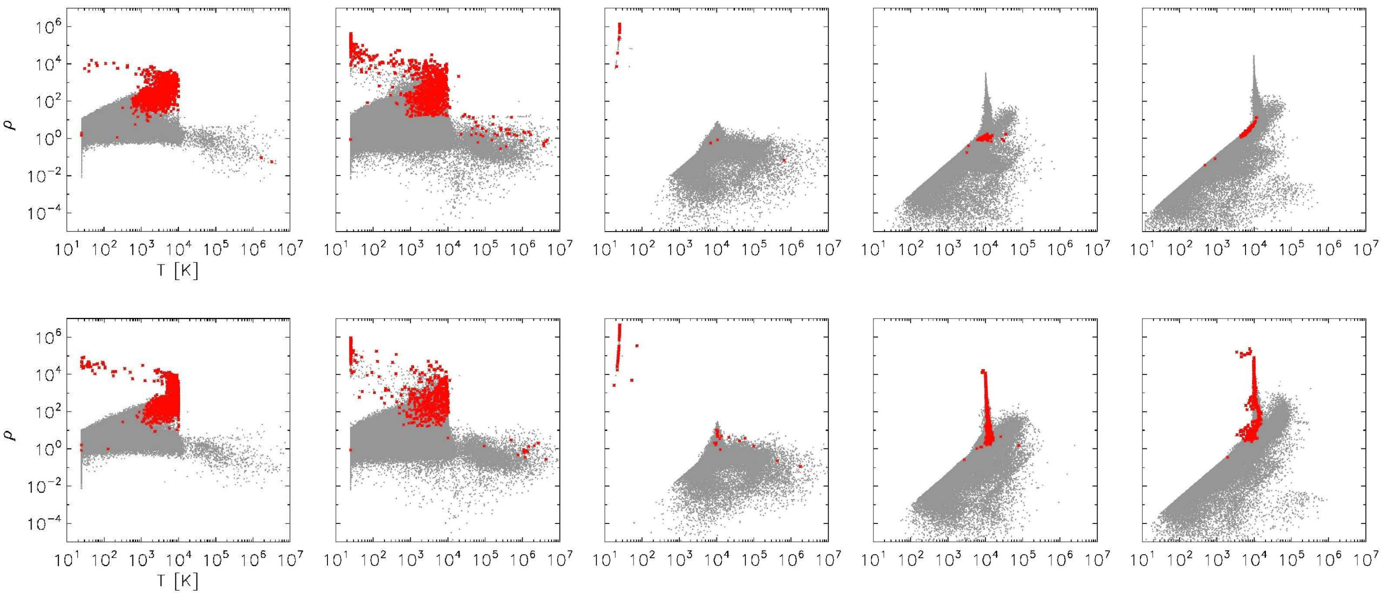

Figure 10. Temperature and density of gas particles. Red dots indicate gas that is bound to the central halo, while grey dots are for particles in all other parts of the simulated volumes. Initial conditions for the simulations are identical to Simulations 2 and 7, shown in the top and bottom rows of Figure 7, respectively, which include supernova feedback, UV radiation and self-shielding, and which reach final halo masses of 3.5×10^{8} and $\sim 9 \times 10^{8} \mathrm{M}_{\odot}$. As a result of additional low temperature cooling in both haloes, early star formation and supernova driven outflows occur at a slightly higher rate. In the low mass case, the subsequent evolution is very similar to the situation shown in the top row of Figure 7 without low-temperature cooling. As in the case without low temperature cooling, the residual amount of gas is again too small to be effectively self-shielding by the time reionization sets in at redshift $z = 6$. In the high mass scenario, the amount of residual gas at $z = 6$ is also reduced with respect to the case without low-temperature cooling, and hence the effect of self shielding is somewhat lower, leading to slightly less subsequent star formation.

that atomic hydrogen cooling alone is not sufficient to form the observed dwarf galaxies, and they as well as other authors (e.g. Mashchenko et al. 2008; Revaz et al. 2009) have found different ways to include low temperature cooling due to molecules and metals in their simulations. By contrast, Mayer et al. (2005) and others have only considered cooling above 10^{4} K. We have repeated several simulations with additional low temperature cooling, using the extended cooling functions of Maio et al. (2007). Figure 10 shows the distribution of gas particles in the temperature-density plane at different redshifts for two simulations with low-temperature cooling. Both simulations have identical initial conditions to Simulations 2 and 7, respectively, and include the full physical model of supernova feedback, UV radiation and self shielding. Figure 10 can be compared to Figure 7, which shows the evolution without low temperature cooling. In each case, with low temperature cooling, star formation proceeds at slightly higher efficiency at high redshifts. As a consequence of supernova feedback acting at a lower halo mass, the interstellar gas mass peaks at higher redshift. For the lower mass scenarios, the effect on the total stellar mass is minimal. In the high mass case, however, the decreased gas mass at $z = 6$ decreases the efficiency of self-shielding against the cosmic UV background, and hence the amount of subsequent star formation.

In general, we find that the inclusion of low-temperature cooling does not have a very strong effect on the formation of dwarf galaxies in the mass range of 10^{8} to $10^{9} \mathrm{M}_{\odot}$, which we have considered in this study, and which have all began to form stars before reionization. It does not qualitatively alter the response of the interstellar medium to supernova feedback or the UV background.

However, we cannot exclude the possibility that low temperature cooling may have a significant effect on the formation and evolution of galaxies with even lower halo masses, whose virial temperatures are far below 10^{4} K. In all of our simulations, we have assumed the gas to be metal-free before the first stars are formed and release metals ab initio. As the cooling function in Figure 1 shows, possible pre-enrichment of the intergalactic medium could enhance the cooling efficiency, which might also play a role in this case.

5 EXPLORING THE PARAMETER SPACE

Even though our model is physically motivated, it also contains a certain degree of parameterisation in addition to the numerical parameters discussed in Section 2, which cannot be determined ab initio in our simulations. We have therefore explored a range of variables that have a direct physical significance, some of which we hope to constrain by comparison with observations, and others that may simply help to explain the variation amongst the observed systems.

5.1 Total Mass: Scaling Relations

Measurements of stellar kinematics of the Local Group dwarf spheroidal and ultra-faint dwarf galaxies have recently re-

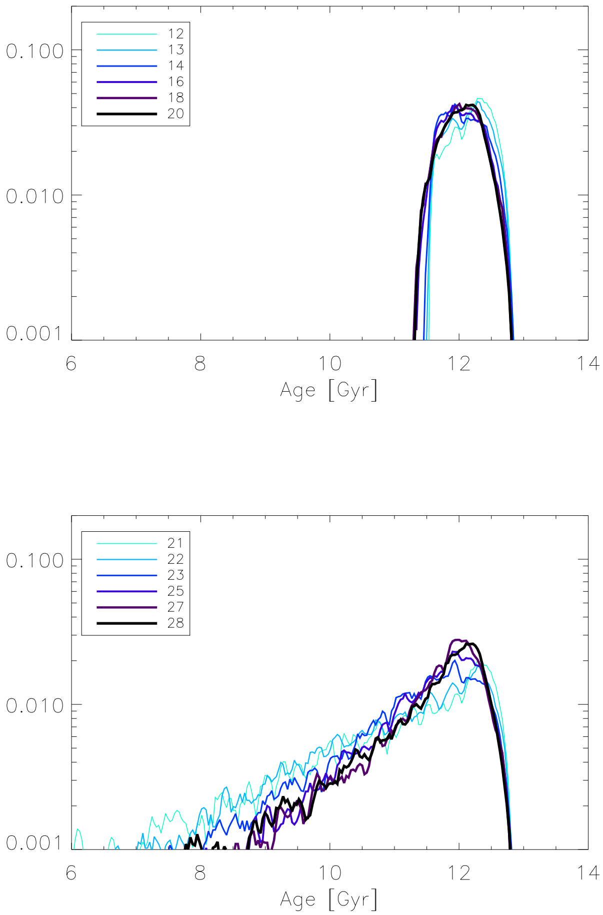

Figure 6. Distribution of stellar ages in Gyr. Simulations of the same halo mass are shown in the same colour in the two panels, darker colours and thicker lines indicate higher mass. A UV background (but no self shielding) is included for simulations 12-20, in the top panel, while the UV background is ignored in simulations 21-28, on the bottom. The final halo masses range from $2.3\times10^8\mathrm{M}_\odot$ (simulations 12 and 21, lightest blue) to $1.2\times10^9\mathrm{M}_\odot$ (simulations 20 and 28, black). Other properties of the simulations are summarised in Table 1.

vealed a striking similarity in the inferred virial mass contained within the central 300 pc. It is consistent with a common value of $10^7\mathrm{M}_\odot$ over several orders of magnitude in luminosity (Strigari et al. 2008). This suggests that all dwarf spheroidals reside in similar dark matter haloes. Why then do they have such a large variation in stellar mass?

Some of the effects of the depth of the potential well have already been described in Sections 4.2 and 4.3, reflecting the fact that no parameter can really be studied in isolation. In this section, we look at the series of simulations that includes all of the physical processes: cooling, star formation, feedback, UV radiation and self-shielding, but focus on a comparison with the observed scaling relations. As described in Section 2.5, we have scaled the initial conditions at constant density, which results in final virial masses between 2.3 $\times10^8$ and 1.2 $\times10^9\mathrm{M}_\odot$. This corresponds to masses within 300 pc between 0.9 $\times10^7$ and 1.8 $\times10^7\mathrm{M}_\odot$, similar to those obtained by Strigari et al.. We nevertheless find a surprisingly large variation in stellar mass, luminosity, central mass to light ratio and metallicity, as summarised in Table 1. The final stellar masses range between 5.5×10^5 and $1.2\times10^7\mathrm{M}_\odot$, whilst the median iron abundance ranges from [Fe/H] $= -1.78$ to -1.12.

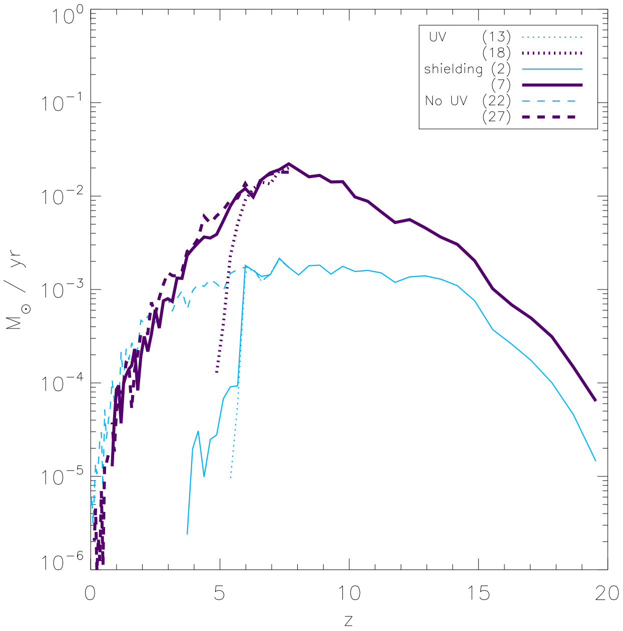

Figure 8. Star formation rate in $\mathrm{M}_\odot$ yr^{-1}, for a total of six simulations in two groups of different halo masses. Simulations 2, 13 and 22, which have a final halo mass of $\sim 3.5\times10^8\mathrm{M}_\odot$, are plotted as thick blue lines, while simulations 7, 18 and 27 reach $\sim 9\times10^8\mathrm{M}_\odot$, and are plotted as thin purple lines, in correspondence to the colours used in Figures 6 and 9 for the same masses. All simulations include supernova feedback, they differ in the treatment of the UV background and/or self-shielding. Simulations 22 and 27 (dashed lines) include no UV radiation. Simulations 13 and 18 (dotted) include a UV background, and simulations 2 and 7 (solid) also include self-shielding. It can be seen that the star formation rates for all systems of a given mass are identical up to redshift $z = 6$. After that, for both masses, they decline sharply in the scenarios with UV background and no shielding (dotted), and more gradually when the UV background is ignored (dashed). However, the impact of self-shielding (solid) is different for the two masses. In the high mass halo, the result with self-shielding resembles the case without UV radiation, whereas in the low-mass halo, the star formation rate drops almost as sharply with self-shielding as without.

In Figure 11, we show that this is sufficient to reproduce the well-known mass-metallicity relation (e.g. Mateo 1998) of dwarf spheroidals. We compare the results from our simulations, shown as red open squares, to those of 14 'classical' Local Group dwarf spheroidals, as given by Woo et al. (2008), overplotted as black triangles. We find that there is good agreement, both in the range of metallicities obtained, as well as in the slope of the relation, and that this is not affected by resolution.

We also show the distributions of metallicities of individual star particles per galaxy in Figure 12. Comparing this with observed distributions, e.g. by Helmi et al. (2006), we

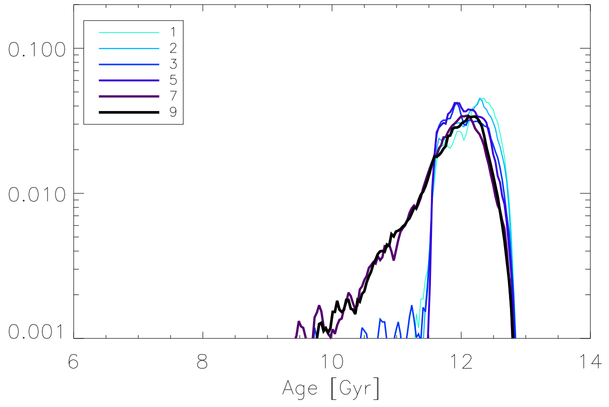

Figure 9. Distribution of stellar ages in Gyr, in simulations 1-9, which include feedback, a UV background and self-shielding, as described in the text. As in Figure 6, the colours and line strengths indicate different halo masses, from $2.3 \times 10^8 \mathrm{M}_\odot$ (simulation 1, lightest blue) to $1.2 \times 10^9 \mathrm{M}_\odot$ (simulation 9, black). Other properties are listed in Table 1. While simulations 1-5 show only an old stellar population, similar to the top panel of Figure 6, a transition occurs around a final halo mass of $\sim 8 \times 10^8 \mathrm{M}_\odot$, above which self-shielding becomes effective, allowing star formation to continue beyond $z = 6$.

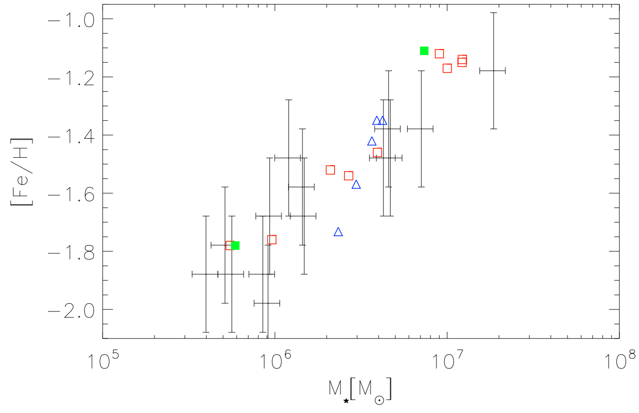

Figure 11. Mean metallicity and stellar mass for 14 observed dwarf spheroidals, in black with error bars, together with the results from our simulations. Red squares show a sequence of simulations (1-9) with varying initial masses, which gives a good fit to the observations. Also shown, with blue triangles, is a sequence of simulations with varying parameters of $c_\star$. While it intersects with the observed relation, the slope is much too steep compared with observations. The two filled, green squares are the results of two simulations with increased resolution, as discussed in Section 2.6. The observational uncertainties, as given by Woo et al., are 0.2 dex for [Fe/H] and 0.17 dex for stellar mass.

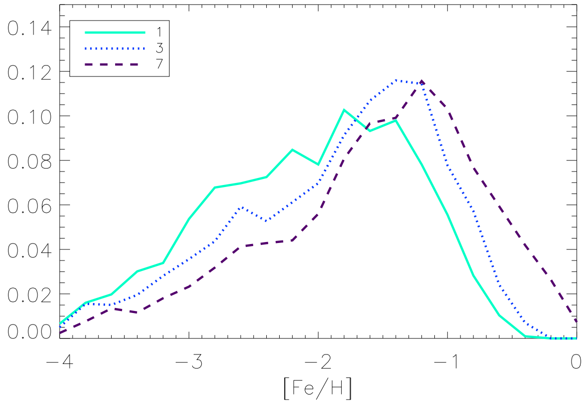

Figure 12. Relative, mass-weighted metallicity distribution of individual stars for the three simulations 1, 4 and 7, which vary in final halo mass.

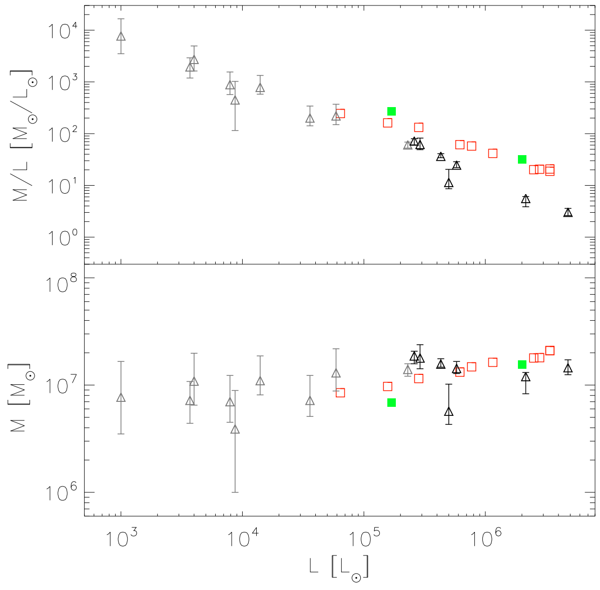

Figure 13. Mass-to-light ratio within 300 pc as a function of total luminosity. Simulations 1 through 9 from Table 1 and one additional, lower mass simulation are plotted as red squares, together with the 8 'classical' Milky Way satellites and the 10 'SDSS Dwarfs' contained in the analysis of Strigari et al., in black and grey triangles with error bars, respectively. The two filled, green squares are the results of two simulations with increased resolution discussed in Section 2.6.

find an overabundance of both metal-rich and metal-poor stars for a given median metallicity. We attribute this to a lack of dissipative metal-mixing in the interstellar medium of our simulations. As a result, pockets of relatively metal-poor (or metal-rich) gas survive longer, and are able to form more stars of corresponding metallicity, which is reflected in a comparatively broad stellar metallicity distribution, as well as steeper negative metallictity gradients compared with observations.

In Figure 13 we compare the same set of simulations to observed Milky Way satellite galaxies in terms of their luminosities and mass-to-light ratios. The observational sample is identical to the one used by Strigari et al. (2008), and comprises 8 'classical' dwarf spheroidals, as well as 10 of the newly-discovered ultra-faint galaxies (Willman et al. 2005; Belokurov et al. 2007). While the observed galaxies span an even larger range in luminosity than the ones we have simulated, we find a similar, tight inverse correlation between luminosity and mass-to-light ratio. Whereas Strigari et al. find only a very weak dependence $M_{0.3} \propto L^{0.03 \pm 0.03}$, our relation is somewhat steeper at $M_{0.3} \propto L^{0.24}$. This is still a remarkably weak dependence, and it allows us to reproduce a large range in luminosity with an $M_{0.3}$ mass that varies by only a factor of two. As we discuss below, the remaining difference may point to the fact that our model does not yet include all physical effects, and that our assumption of an underlying mass distribution is not the full story. Strigari et al. also note that for the most luminous dwarf spheroidals such as Fornax, the mass-to-light ratios relating the mass within 300 pc to the total luminosity in the observed galaxies tend to be underestimates, since their stellar populations are typically more extended.

5.2 Kinematics

As shown in Table 1, the mean one-dimensional velocity dispersions in each galaxy resulting from our simulations are in the range of 6.5 to 9.7 kms^{-1}. This is comparable to the observed range of 7 to 10 kms^{-1} for six of the seven ‘classical’ Local Group dwarf spheroidals in the sample of Walker et al. (2007). The one exception, Fornax, has a velocity dispersion of about 12 kms^{-1}. Its stellar population, which includes several globular clusters, is more spatially extended, and its stellar mass is also slightly higher than that of the most luminous galaxy in our simulations. At the faint end, an extrapolation of our results might also be consistent with the corresponding values of the eight ultra-faint Milky Way satellites presented in Simon & Geha (2007), which have velocity dispersions between 3.3 and 7.6 kms^{-1}.

We also investigated the influence of supernova feedback on the shape of the dark matter distribution. It is still an open question whether flat cores, rather than the cusps predicted by dissipationless cold dark-matter models exist in the central regions of dwarf galaxy haloes. While for a stellar system with uniform mass-to-light ratio, the shape of the gravitational potential can be uniquely determined from the observed velocity dispersion and surface brightness profiles, in the case of the highly dark-matter dominated dwarf spheroidal galaxies, the unknown mass-to-light ratios result in a degeneracy between the gravitational potential variation and the velocity anisotropy (Dejonghe & Merritt 1992). The same data, when analysed with different anisotropy assumptions, can therefore result in different density profiles, and as Van den Bosch & Swaters (2001) and Evans et al. (2008) have shown, the stellar kinematics of dwarf spheroidal galaxies are generally not sufficient to distinguish between cored and cusped profiles. Nevertheless, reports of central-density cores in dwarf galaxies (e.g. Carignan & Beaulieu 1989; de Blok et al. 2001; Łokas 2002) have been considered as evidence for warm dark-matter (e.g. Moore 1994). Within the framework of ΛCDM, numerical simulations by Navarro et al. (1996), Read & Gilmore (2005), Mashchenko et al. (2008) and others have suggested that cores of kpc scale may form either as a result of dynamical coupling to supernova-induced bulk gas motions, or the rapid ejection of large amounts of baryonic matter. Our simulations fail to fulfil these requirements in two ways. The ejection of gas is not sufficiently rapid (which would also be difficult to reconcile with the observed age-spreads), and our dark matter haloes continue to evolve and grow after star formation and supernova rates have peaked, instead of simply settling to an equilibrium configuration. As a result, we do not observe the formation of cores in our runs with feedback. The final dark matter density distributions can be described by NFW-profiles up to the resolution limit.

5.3 Star Formation Efficiency

We have also run a number of simulations where we have varied the star-formation parameter $c_\star$, the constant of proportionality that enters the Schmidt law for the rate at which cold gas gets turned into stars (see Section 2.2). When the star formation is parameterized in this way in galactic chemical evolution models for late-type galaxies, the choice of $c_\star$ has a strong influence on the star formation rate (Ferreras & Silk 2001), and hence the stellar age distribution, as well as on the final stellar mass. We find no such strong influence in our simulated dwarf spheroidals, in agreement with Katz et al. (1996) and others. The star formation rate increases with $c_\star$ at all redshifts, and as a result, the final stellar mass scales as roughly $M_\star \propto c_\star^{0.25}$ over the range of $c_\star$ between 0.01 and 0.1. In the example of initial conditions identical to simulation 4 in Table 1, this corresponds to a range in final stellar masses of 2.3 to $4.2 \times 10^6 \mathrm{M}_\odot$. This relatively weak dependence points to the fact that in dwarf galaxies, the main factor that determines the overall star formation is not the specific efficiency of turning cold gas into stars, but the amount of feedback and UV heating they can sustain before star formation gets shut down, which in our models strongly depends on the depth of the potential well.

There is nevertheless some degeneracy between star formation efficiency and halo mass when it comes to the amount of stars formed. This can be broken partially by considering chemical evolution. In Figure 11 we have included a simulation sequence of differing star formation efficiency but identical initial conditions, represented by blue diamonds, and we compare it to the observed mass-metallicity relation, as well as to the relation obtained from the sequence of simulations with varying total masses. Besides the much narrower range in stellar mass of the $c_\star$ sequence, its slope is also too steep when compared with observations, which in contrast, are well-matched by the varying mass sequence. While the amount of scatter prevents us from selecting a particular value of $c_\star$, it appears that the range in luminosities and the mass-metallicity relation cannot be explained by a simple scaling of the star formation efficiency. For most of our simulations, we have adopted a value of $c_\star = 0.05$, in agreement with Stinson et al. (2007) and Mashchenko et al. (2008).

5.4 Supernova-progenitor lifetimes

Our feedback model includes both supernovae type II and type Ia. The delay time of supernovae type II is theoretically constrained to be on the scale of Myrs, but due to the uncertain nature of their progenitors, that of supernovae type Ia is much more uncertain. We find that in our simulations, the bulk of the thermal feedback released in time to influence the star formation history is provided by supernovae

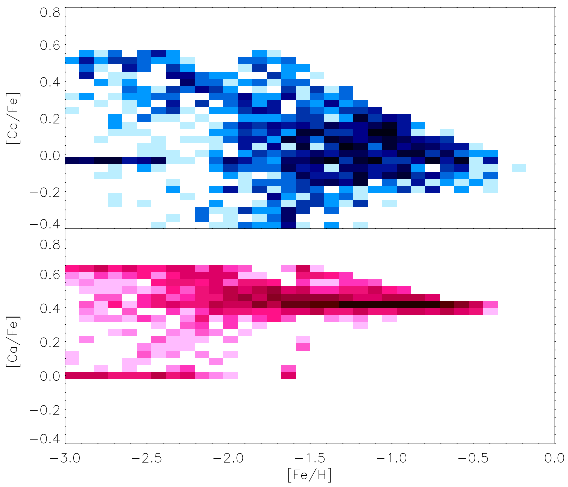

Figure 14. Abundance ratios of [Ca/Fe] vs [Fe/H] of the stars, in simulations with a minimum supernova Ia lifetime of 10^8 years (top) and 5×10^8 years (bottom). The distribution shown on top is for simulation 1, and shows the characteristic drop due to the transition from pure type II to type Ia element ratios. The second simulation is identical to simulation 1 in all other parameters, but due to the increased lifetime of the SN type Ia progenitors, the relative abundances remain fixed at the SN type II ratios.

type II. However, the delay time for supernovae type Ia influences both the total iron enrichment, and the position of the turnover point on the [α/Fe] / [Fe/H] diagram. In dwarf spheroidal galaxies with very short star formation episodes, this effect is particularly strong. In all simulations presented in this work, we assume a uniform delay time distribution with a maximum delay time of 1 Gyr. We have performed simulations with minimum delay times between 100 Myrs and several Gyrs, and found that once the minimum lifetime is increased above several hundred Myrs, the [α/Fe] ratios are too high, and there is no visible turnover point on the [α/Fe]/[Fe/H] diagram, contrary to the observed distribution of red giants in Local Group dwarf spheroidals (e.g. Shetrone et al. 2003; Tolstoy et al. 2003). The two scenarios are illustrated in Figure 14, which shows the [Ca/Fe] ratios for minimum lifetimes of 10^8 years (upper panel) and 5×10^8 years (lower panel) in two simulations with initial conditions identical to simulation 2 in Table 1 that both have an age-spread of ~ 1.1 Gyrs. With a more careful analysis and better constraints on other aspects of the chemical evolution model, such as the mixing of elements, the initial mass function and the yields, those dwarf spheroidal galaxies which show evidence for enrichment by type Ia supernovae despite an apparently short star-forming phase might therefore provide an upper bound on the minimum lifetime of supernova type Ia progenitors. On the other hand, we are satisfied that allowing the lifetime to be a 'free parameter' of the model, the best fit to the observations is obtained with a minimum lifetime of around 100 Myrs, compatible with the value suggested by Matteucci & Recchi (2001).

6 SUMMARY

We have studied the formation and evolution of dwarf galaxies with halo masses in the range of $\sim 2 \times 10^8$ to 10^9 $\mathrm{M}_\odot$ in full cosmological simulations including cooling, supernova feedback and UV radiation. Our models have resulted in the formation of galaxies similar to the Local Group dwarf spheroidals. They span a wide range in luminosity, 6.4×10^4 to 3.4×10^6 $\mathrm{L}_\odot$ and median metallicity, from [Fe/H]$= -1.83$ to -1.12. The variation in total mass, 2.3 to 11.8 $\times 10^8$ $\mathrm{M}_\odot$, is surprisingly small, but it is comparable to the values inferred from observations in the Local Group. The range of velocity dispersions, 6.5 to 9.7 kms^{-1}, is also in good agreement with the observed range. Our simulations have resulted in two kinds of age distributions, either a single burst of star formation lasting around 1 Gyr, or a burst followed by a tail extending over several Gyrs. Both of these have Local Group analogues. However, in some sense the sample of dwarf spheroidal galaxies in the Local Group is even more diverse. Our limited set of initial conditions did not produce a system as luminous and extended, or with such a large age-spread as Fornax, nor were we able to resolve systems as faint as some of the ultra-faint dwarf galaxies.

We have shown that in our simulations, feedback from supernovae and the cosmic UV background shape both the dynamical and the chemical evolution of dwarf spheroidal galaxies. As a result, these are inseparably linked, which is reflected in the scaling laws such as the mass-metallicity relation. Feedback is essential for the evolution of all galaxies in our models, while additional UV radiation is required to reproduce the full range of observed galaxies, particularly those which only have a short burst of star formation. We have demonstrated that, with a sensible choice of parameters, the formation of systems comparable to Local Group dwarf spheroidal galaxies is possible. While we stress that we do not suggest that the dwarf spheroidal population in the Local Group reflects merely a variation in halo mass, we conclude that it is possible to reproduce the wide range of observed stellar masses and metallicities, as well as differing star formation histories within a single evolutionary scenario, and for a narrow range of dynamical masses, as observed.

Our simulations put the Local Group dwarf galaxies in a unique position where the gravitational potential is at a critical value with respect to the combined effects of supernova feedback and UV heating. We find that both are necessary to reproduce the observations. In this scenario, a number of dynamical and stellar evolution effects conspire to reproduce the observed scaling relations. More massive galaxies start off with a proportionally higher initial gas mass, and in addition turn a larger fraction of it into stars, because their deeper potential wells moderate supernova-driven outflows and also allow the gas to self-shield against the UV background. On top of that, more efficient recycling of the gas leads to higher metallicities, and a more extended star formation history results in a younger stellar population with higher specific luminosities. While all these effects undoubtedly play a role in the real systems, differing assembly and accretion histories, and differing environments are likely also to influence dwarf spheroidal structure.

With regard to the 'laboratory' characteristics of dwarf spheroidals mentioned in our introduction and underlined by our results, as well as in view of the enormous difference in scale compared with the disk galaxies studied by Scannapieco et al. (2008), the addition of low-temperature cooling and self-shielding has relatively minor effects. It is a noteworthy and reassuring result that the same numerical model effectively works for both kinds of galaxies. Our models do not yet include the mixing of elements in the interstellar medium, or cooling outside the collisional excitation equilibrium. In addition, their environment differs from the Local Group, where environmental effects are clearly reflected in relations such as the apparent dependence of star-formation timescale on Galactic distance (Van den Bergh 1994; Grebel 1997). Nevertheless, it remains to be seen how important they are compared to feedback and the UV background. Our choice of initial mass function has produced a residual population of metal-free stars in the simulations, which are not observed. The inclusion of early enrichment by Population III stars might remove this discrepancy. Simulations by Wise & Abel (2008) have recently studied how massive Population III stars, and the resulting photoionization at redshifts ~ 30 may affect the interstellar medium in dwarf galaxies. This would be an interesting addition to our models. Addressing these issues should lead to a more complete understanding of the evolution of dwarf galaxies, and should also allow us to make more detailed comparisons with individual objects, exploiting the high quality data that have become available in recent years.

ACKNOWLEDGEMENTS

We would like to thank Volker Springel for his support with the numerical methods that made this work possible, and Adrian Jenkins for his advice and for preparing the initial conditions. We also thank Pascale Jablonka for her advice, which was essential to this and to earlier work. Finally, we would like to thank our anonymous referee for his comments, which have improved the quality of this work. The simulations were carried out at the computing centre of the Max-Planck Society in Garching.

REFERENCES

Battaglia, G. et al. 2006, A&A, 459,423
Belokurov, V. et al. 2007 ApJ, 654, 897
Bolton, J., Meiksin, A. and White, M. 2004, MNRAS, 348, 43
Bromm, V. and Clarke, C. J. 2002, ApJ, 566, 1
Bruzual, G. and Charlot, S. 2003, MNRAS, 344, 1000
Bush, S. J., Cox, T. J., Hernquist, L., Thilker, D. and Younger, J. D. 2008 ApJ, 683, 13
Carignan, C. and Beaulieu, S. 1989, ApJ, 347, 760
Castellani, M., Marconi, G. and Buonanno, R. 2006, A&A, 310, 715
Chapman, S. C. et al. 2008, ApJ, 662, L79
Ciardi, B., Ferrara, A. and White, S. D. M. 2003, MNRAS, 344, L7
Colín, P., Klypin, A., Valenzuela, O. and Gottlöber, S. 2004, ApJ, 612, 50C
Dalgarno, A. and McCray, R. A. 1972, ARA&A, 10, 375
Dalla Vecchia, C. and Schaye, J. 2008, MNRAS, 387, 1431
de Blok, W. J. G., McGaugh, S. S. , Bosma, A. and Rubin, V. C. 2001, ApJ, 552, 23
Dejonghe, H. and Merritt, D. 1992, ApJ, 391, 531
Dekel, A. and Silk, J. 1986, ApJ, 303, 39
Diemand, J., Kuhlen, M. and Madau, P. 2007, ApJ, 667, 859
Efstathiou, G. 1992, MNRAS, 256, 43
Evans, N. W., An, J. and Walker, M. G. 2008, MNRAS, accepted
Faber, S. M. and Lin, D. N. C. 1983, ApJ, 266. 17
Fan, X. Narayanan, V. K. Strauss, M. A. White, R. L. Becker, R. H. Pentericci, L. and Rix, H.-W. 2002, AJ, 123, 1247
Ferrara, A. and Tolstoy, E. 2000, MNRAS, 313, 291
Ferreras, I. and Silk, J. 2001, ApJ, 557,165
Fraternali, F., Tolstoy, E., Irwin, M. and Cole, A. 2009, arXiv 0903.4635
Goerdt, T., Moore, B., Read, J. I., Stadel, J. and Zemp, M. 2006, MNRAS, 368, 1073
Governato, F., Willman, B., Mayer, L., Brooks, A., Stinson, G., Valenzuela, O., Wadsley, J. and Quinn, T. 2007, MNRAS, 374, 1479
Grebel, E. K. 1997, Reviews in Modern Astronomy, 10, 29
Grebel, E. K. and Gallagher, III, J. S. 2004, ApJ, 610, L89
Haardt, F. and Madau, P. 1996, ApJ, 461, 20
Hayashi, E. et al. 2003, MNRAS, 355, 794
Helmi, A. et al. 2006, ApJ, 651, L121
Hoeft, M., Yepes, G., Gottlöber, S. and Springel, V. 2006, MNRAS, 371, 401
Hoeft, M., Yepes, G. and Gottlöber, S. 2008, IAU Symposium, 244, 279
Katz, N. 1992, ApJ, 391, 502
Katz, N., Weinberg, D. H. and Hernquist, L. 1996, ApJS, 105, 19
Kennicutt, Jr., R. C. 1989, ApJ, 344, 685
Kennicutt, Jr., R. C. 1998, ApJ, 498, 541
Kitayama, T., Tajiri, Y., Umemura, M., Susa, H. and Ikeuchi, S. 2000, MNRAS, 315, L1
Klypin, A., Kravtsov, A. V., Valenzuela, O. and Prada, F. 1999 ApJ, 522, 82
Koch, A.. Grebel, E. K., Wyse, R. F. G., Kleyna, J. T., Wilkinson, M. I., Harbeck, D. R., Gilmore, G. F. and Evans, N. W. 2006, AJ, 131, 895
Koch, A., Kleyna, J. T., Wilkinson, M. I., Grebel, E. K., Gilmore, G. F., Evans, N. W., Wyse, R. F. G., Harbeck, D. R. 2007, AJ, 134, 566
Koch, A., Grebel, E. K., Gilmore, G. F., Wyse, R. F. G., Kleyna, J. T., Harbeck, D. R., Wilkinson, M. I. and Evans, N. W. 2008, AJ, 135, 1580
Koyama, H. and Ostriker, E. C. 2009, ApJ, 693, 1316
Lewis, G. F., Ibata, R. A., Chapman, S. C., McConnachie, A., Irwin, M. J., Tolstoy, E. and Tanvir, N. R. 2007, MNRAS, 375, 1364
Li, Y.-S. and Helmi, A. 2008, MNRAS, 385, 1365
Łokas, E. L. 2002, MNRAS, 333, 697
Maio, U., Dolag, K., Ciardi, B. and Tornatore, L. 2007, MNRAS, 379, 963
Marlowe, A. T., Heckman, T. M., Wyse, R. F. G. and Schommer, R. 1995, ApJ, 438, 563
Marri, S. and White, S. D. M. 2003, MNRAS, 345, 561
Martin, N. F., Ibata, R. A., Irwin, M. J., Chapman, S., Lewis, G. F., Ferguson, A. M. N., Tanvir, N. and Mc-

Connachie, A. W. 2006, MNRAS, 371, 1983
Mashchenko, S., Wadsley, J. and Couchman, H. M. P. 2008, Science, 319, 174
Mateo, M. L. 1998, ARA&A, 36, 435
Mateo, M. and Olszewski, E. W. and Walker, M. G. 2008, ApJ, 675, 201
Matteucci, F. and Recchi, S. 2001, ApJ, 558, 351
Mayer, L., Mastropietro, C., Wadsley, J., Stadel, J. and Moore, B. 2005, MNRAS, 369, 1021
Moore, B. 1994, Nature, 370, 629
Moore, B. 1999, ApJ, 524, 19
Nagai, D. and Kravtsov, A. V. 2005, ApJ, 618, 557
Navarro, J. F., Eke, V. R. and Frenk, C. S. 1996, MNRAS, 283, 72
Navarro, J. F., Frenk, C. S. and White, S. D. M. 1997, ApJ, 490, 493
Navarro, J. F. and White, S. D. M. 1994, MNRAS, 267, 401
Orban, C., Gnedin, O. Y., Weisz, D. R., Skillman, E. D., Dolphin, A. E. and Holtzman, J. A. 2008, ApJ, 686, 1030
Quirk, W. J. 1972, ApJ, 176, 9
coolin
Read, J. I. and Gilmore, G. 2005, MNRAS, 356, 107
Read, J. I., Pontzen, A. P. and Viel, M. 2006, MNRAS, 371, 885
Revaz, Y. et al. 2009, A&A(accepted)
Salpeter, E. E. 1955, ApJ, 121, 161
Scannapieco, C., Tissera, P. B., White, S. D. M. and Springel, V. 2005, MNRAS, 364, 552
Scannapieco, C., Tissera, P. B., White, S. D. M. and Springel, V. 2006, MNRAS, 371, 1125
Scannapieco, C., Tissera, P. B., White, S. D. M. and Springel, V. 2008, MNRAS, 389, 1137
Scannapieco, C., White, S. D. M., Springel, V. and Tissera, P. B. 2009, arXiv 0812.0976
Shetrone, M., Venn, K. A., Tolstoy, E., Primas, F., Hill, V. and Kaufer, A. 2003, AJ, 125, 684
Simon, J. D. and Geha, M. 2007, ApJ, 670, 313
Somerville, R. S. 2002, ApJ, 572, 23
Springel, V. and Hernquist, L. 2003, MNRAS, 339, 289
Springel, V. 2005, MNRAS, 364, 1105
Springel, V. et al. 2008, MNRAS(submitted)
Stinson, G. S., Dalcanton, J. J., Quinn, T., Kaufmann, T., Wadsley, J. 2007, ApJ, 667, 170
Stinson, G. S., Dalcanton, J. J., Quinn, T., Gogarten, S., Kaufmann, T., Wadsley, J. 2009, arXiv 0902.0075
Strigari, L. E., Bullock, J. S., Kaplinghat, M., Simon, J. D., Geha, M., Willman, B. and Walker, M. G. 2008, Nature, 454, 1096
Susa, H. and Umemura, M. 2004, ApJ, 600, 1
Sutherland, R. S. and Dopita, M. A. 1993, ApJS, 88, 253
Tajiri, Y. and Umemura, M. 1998, ApJ, 502, 59
Thacker, R. J. and Couchman, H. M. P. 2000, ApJ, 545, 728
Tollerud, E. J., Bullock, J. S., Strigari, L. E. and Willman, B. 2008, ApJ, 688, ,277
Tolstoy, E., Venn, K. A., Shetrone, M., Primas, F., Hill, V., Kaufer, A. and Szeifert, T. 2003, AJ, 125, 707
Van den Bergh, S. 1994, ApJ, 428, 617
Van den Bosch, F. C. and Swaters, R. A. 2001, MNRAS, 325, 1017
Thielemann, F. K., Nomoto, K., Hashimoto, M. 1993, in Prantzos N., Vangoni-Flam E., Casse, N., eds, Origin and Evolution of the Elements. Cambridge Univ. Press, Cambridge, p. 299
Valcke, S., de Rijcke, S., Dejonghe, H. 2008, MNRAS, 389, 1111
Walker, M. G., Mateo, M., Olszewski, E. W., Gnedin, O. Y., Wang, X., Sen, B., Woodroofe, M. 2008, ApJ, 667, 53
Walker, M. G., Mateo, M. and Olszewski, E. W. 2009, AJ, 137, 3100
Wiersma, R. P. C., Schaye, J. and Smith, B. D. 2009, MNRAS, 393, 99
Willman, B. et al. 2005, ApJ, 626, L85
Wise, J. H. and Abel, T. 2008, ApJ684, 1
Wise, J. H. and Abel, T. 2008, ApJ, 685, 40
Woo, J., Courteau, S. and Dekel, A. 2008, MNRAS, online early
Woosley, S. E. and Weaver, T. A. 1995, ApJS, 101, 181